Crystallization of Binary Nanocrystal Superlattices and the Relevance of Short-Ranged Attraction

Emanuele Marino,[1,8,‡] R. Allen LaCour,[4,‡] Timothy C. Moore,[4] Sjoerd W. van Dongen,[1,6] Austin W. Keller,[2] Di An,[1] Shengsong Yang,[1] Daniel J. Rosen,[2] Guillaume Gouget,[1] Esther H.R. Tsai,[7] Cherie R. Kagan,[1,2,3] Thomas E. Kodger,[6] Sharon C. Glotzer,[4,5,] and Christopher B. Murray[1,2,*]*

[1]Department of Chemistry, [2]Department of Materials Science and Engineering, [3]Department of Electrical and Systems Engineering, University of Pennsylvania. Philadelphia, Pennsylvania, 19104, United States.

[4]Department of Chemical Engineering and [5]Biointerfaces Institute, University of Michigan, Ann Arbor, Michigan 48109, United States.

[6]Physical Chemistry and Soft Matter, Wageningen University and Research, 6708WE, Wageningen, The Netherlands.

[7]Brookhaven National Laboratory, Bldg. 735, Center for Functional Nanomaterials, Upton, NY 11973-5000, USA.

[8]Dipartimento di Fisica e Chimica, Università degli Studi di Palermo, Via Archirafi 36, 90123 Palermo, Italy.

ABSTRACT

The synthesis of binary nanocrystal superlattices (BNSLs) enables the targeted integration of orthogonal physical properties, such as photoluminescence and magnetism, into a single superstructure, unlocking a vast design space for multifunctional materials. However, the formation mechanism of BNSLs remains poorly understood, restricting the prediction of the structure and properties of superlattices. Here, we use a combination of *in situ* scattering and molecular simulation to elucidate the self-assembly of two common BNSLs (AlB_2 and $NaZn_{13}$) through emulsion templating. Our self-assembly experiments reveal that no intermediate structures precede the formation of the final binary phases, indicating that their formation proceeds through classical nucleation. Using simulations, we find that, despite the formation of AlB_2 and $NaZn_{13}$ typically being attributed to entropy, their self-assembly is most consistent with the nanocrystals possessing short-range interparticle attraction, which we find can accelerate nucleation kinetics in BNSLs. We also find homogenous, classical nucleation in simulation, corroborating our experiments. These results establish a robust correspondence between experiment and theory, paving the way towards prediction of BNSLs.

Introduction

Recent advances have enabled the synthesis of colloidal nanocrystals (NCs) with different sizes, shapes, and compositions, generating a library of nanoscale building blocks with well-defined optical, electronic, and magnetic properties. These properties have been exploited to develop optoelectronic devices like photodetectors,[1,2] light-emitting diodes,[3,4] field-effect transistors,[5,6] and solar cells[7,8] by assembling NCs into ordered solids, or superlattices. While single-component NC superlattices have already revealed structure-property relationships,[9,10] multi-component NC

superlattices are still in the early stages of investigation.[11] The integration of NCs with orthogonal functionalities is crucial in unlocking a vast synthetic design space for material properties resulting from the synergistic interaction of the individual components.[12-20] So far, the exploration of this design space has been restricted by our limited understanding of the formation of multi-component NC superlattices.

Binary nanocrystal superlattices (BNSLs) with diverse crystal structures have been synthesized, integrating combinations of semiconducting, magnetic, and metallic NCs.[21-23] However, predicting which binary structure self-assembles from a given combination of NCs has proven extremely challenging.[24] With rare exceptions,[25-27] simulation models of binary mixtures of NCs frequently fail to self-assemble, indicating that the current understanding of how NC interactions contribute to the synthesis of BNSLs is incomplete. By contrast, experimental *in situ* studies have already revealed the self-assembly mechanism of single-component NC superlattices,[28-36] enabling *a prior*i structure prediction by capturing both kinetic and thermodynamic aspects of how different inter-NC interactions influence crystallization.[37-43] Yet, in almost two decades since the first observation of BNSLs,[21] only one *in situ* study has focused on mono-functional BNSLs,[44] while no *in situ* studies have investigated the synthesis of multi-functional BNLSs.

Here we combine experiments and simulations to understand the synthesis of multi-functional BNSLs from a combination of magnetic, semiconducting, and plasmonic NCs. A combination of magnetic and semiconducting NCs may prove crucial in modulating the temperature of the atomic lattice and the conductivity of charge carriers.[45,46] Instead, a combination of magnetic and plasmonic NCs may allow active control over the coherent oscillations of charge carriers and the optical response of the material.[47,48] We use synchrotron-based *in situ* small-angle X-ray scattering (SAXS) to follow in real-time the self-assembly of BNSLs isostructural to AlB_2 and $NaZn_{13}$. The

NCs were confined to emulsion droplets that were slowly dried to trigger crystallization, resolving with unprecedented detail the formation of high-quality BNSLs.[28,49-51] This approach was combined with molecular dynamics (MD) simulations to determine the interparticle interactions allowing the formation of these BNSLs. In contrast to some reports of single-component superlattices,[28,30,31,52] we find that nucleation occurs classically for both superlattices, although significant structural compression occurs after nucleation, indicating that the ligands are still swollen with solvent at the time of nucleation. In our MD simulations, we find that, despite the self-assembly of AlB_2 and $NaZn_{13}$ typically being attributed to entropy, only NCs interacting with a short-ranged attraction between NCs results in self-assembly behavior consistent with experiment. Specifically, we find that short-range attraction can dramatically accelerate the crystallizations kinetics of BNSLs. By establishing a direct link between experiments and simulations, our work provides crucial insights into the synthesis of BNSLs, providing a significant step towards the targeted synthesis and *a priori* structure prediction of these complex, 3D artificial solids.

Results and Discussion

We synthesize BNSLs by the self-assembly of binary mixtures of NCs using emulsion-templating,[49,53] which has recently emerged as a consistent and scalable method to fabricate 3D single-component NC superlattices.[28,29,53-61] We prepare a surfactant-stabilized oil-in-water emulsion containing a dispersion of larger (L) super-paramagnetic Fe_3O_4 and smaller (S) semiconductor PbS NCs with an effective size ratio of 0.56, a number ratio of 1:2, and a total inorganic volume fraction of $\phi = 0.001$; see Figures S1-S3 for NC characterization. To collect *in situ* scattering patterns, we flow the emulsion in a closed loop through a quartz capillary aligned with the X-ray beam; see Figure S4 for a schematic of the setup.[28,57] As the volatile oily phase

evaporates, ϕ increases with time. Figure 1a and Movie S1 illustrate the continuous kinetic evolution of the structure factor, *S(q)*. Initially, the structure factor is featureless and centered around 1, as expected for a colloidal gas. During the first 3 hours drying the emulsion, broad features arise across the wave vector range, *q*. After 3.6 hours, a succession of sharp peaks suddenly emerges from the background, growing in intensity while shifting with time towards higher *q*. As highlighted in Figure 1b, the shape of the structure factor at 3.6 hours resembles that of a low-density colloidal fluid, but within 0.1 hours rapidly develops into a fully formed diffraction pattern featuring at least 7 sharp peaks from growing crystallites. Immediately thereafter, all peaks shift synchronously toward higher *q*, indicating a contraction of the crystal lattice. We identify the crystal as isostructural to AlB_2 with parameters $a = b \approx c$; see Figure 1c. This structure is characterized by stacked hexagonal layers of the larger NCs intercalated by hexagonal layers of the smaller NCs that occupy the trigonal prismatic voids left by the larger NCs; see schematic in Figure S5.

To understand the formation of these BNSLs, we extract the evolution of the structural parameters from *in situ* measurements as shown in Figure 1d. After nucleation, lattice contraction induces a slow decrease in the surface-to-surface distance between NCs, *d*. This decrease takes place over several hours to reach an inorganic volume fraction of $\phi = 0.357$; see Figure S6. In stark contrast to this steady compression of the lattice, the average crystal size extracted from the Scherrer equation,[62] ξ, increases rapidly: Within 0.1 hours after nucleation, the crystal size increases to reach $\xi \approx 330$ *nm*, corresponding to $\xi/a \sim 23$ unit cells of the BNSL. Eventually, the crystal size slowly decreases to $\xi \approx 280$ *nm* as the result of lattice compression. Interestingly, we notice that the integrated intensity of the 001 and 100 reflections grow at different rates relative to the 101 reflection, see Figures 1b-c. While the relative integrated intensity of the 001 reflection increases

by 63% during assembly, that of the 100 reflection increases by 140%, as shown in Figure S7. This suggests a strong tendency of the AlB_2 crystal to grow along the basal plane rather than along the *c* axis.

Based on these observations, we hypothesize the synthetic mechanism shown in the inset of Figure 1d: Crystallization occurs as a single-step transition from the fluid to the crystalline phase. The relative positions of the diffraction peaks do not change during assembly, implying the absence of intermediate phases between the fluid and the final crystal. This is a simpler process compared to previous reports on the synthesis of single-component NC superlattices reporting crystal-to-crystal transitions.[30,31,52] Crystallization is followed by the continuous compression of the BNSL. We attribute this compression to the evaporation-driven desorption of solvent from the ligand shell of the NCs, consistently with reports on single-component systems.[28,30,57] *Ex situ* TEM confirms the synthesis of 3D colloidal BNSLs, each featuring a distinct set of NC planes, as shown in Figures 1e, S8-S10. The Fourier transform of the BNSL shown in Figure 1e reveals a discrete set of spots, as expected for a crystalline structure. Combining *in situ* and *ex situ* experimental results leads to the structural model shown in Figure 1f. The synthesized BNSLs retain the superparamagnetic character of their larger NC component, while also displaying a reduced magnetic remanence and spin density relative to the single-component superlattice, as shown in Figure S11.

We test the robustness of this approach by using a NC pair with comparable size ratio, number ratio, and initial volume fraction but featuring larger infrared plasmonic CdO NCs co-doped with fluorine and indium (FICO) and smaller infrared semiconductor PbS NCs (optical activity in Figure S3). Under the same synthetic conditions, their assembly in emulsion yields the same AlB_2 BNSL structure with similar kinetics; see Figure S12 and Movie S2. We next target a different BNSL, $NaZn_{13}$, by increasing the number ratio of these FICO and PbS NCs from 1:2 to 1:13. The

experimental structure factor reveals the onset of diffraction peaks from the flat background shortly after 2.3 hours of drying, as shown in Figure 2a-b and Movie S3. The diffraction pattern appears qualitatively different from Figure 1, with at least 10 discernible reflections. A more careful examination of the final diffraction pattern indicates the coexistence of a majority phase isostructural to $NaZn_{13}$ with a minority AlB_2 phase, as shown in Figure 2c. The $NaZn_{13}$ structure consists of a body-centered icosahedral cluster of 13 smaller particles contained within a simple cubic subcell of the larger particles, as illustrated in the inset in Figures 2c and S13.

We study the synchronous evolution of the $NaZn_{13}$ and AlB_2 phases in Figure 2d. The lattice parameters of the two crystalline phases slowly decrease as a function of time, to reach maximum inorganic volume fractions of $\phi = 0.360$ and 0.384 for $NaZn_{13}$ and AlB_2, respectively. Within 0.1 hours after nucleation, the average domain sizes of the $NaZn_{13}$ and AlB_2 phases rapidly increase and saturate at their final values of $\xi \approx 510$ nm and 200 nm, respectively. We quantify the fraction of each crystalline phase by comparing with the assembly performed at a NC number ratio of 1:2, shown in Figure S12. After nucleation, the fraction of both $NaZn_{13}$ and AlB_2 phases quickly increases to reach the values of 0.74 and 0.21, respectively, confirming $NaZn_{13}$ as the majority phase. Interestingly, while the fraction of the AlB_2 phase shows a slow increase in the late stages of the assembly, that of the $NaZn_{13}$ phase shows a comparable decrease. This suggests that even though the $NaZn_{13}$ phase readily nucleates to occupy most of the available volume, this structure might be thermodynamically less stable than AlB_2. The relative strengths of inter-NC interactions may be responsible for shifting this equilibrium towards one specific phase.

Ex situ dark-field STEM confirms the formation of 3D colloidal $NaZn_{13}$ BNSLs; see Figure 2e. The [200] projection clearly illustrates the cubic symmetry of the $NaZn_{13}$ phase, as well as the four-fold symmetry of the smaller NCs surrounding each larger NC; see also Figures S13-S15. In

Figure 2f we illustrate a 3D model of this colloidal BNSL, obtained by carving a sphere out of a $NaZn_{13}$ lattice with experimentally determined structural parameters. We also observe superstructures characterized by a heterostructure of $NaZn_{13}$ with a second phase, shown in Figure 2g, confirming the presence of a minority phase as suggested by SAXS. Due to interference with the adjacent $NaZn_{13}$ phase, we are unable to clearly identify this secondary phase using STEM. However, the results of *in situ* SAXS suggest the secondary phase should correspond to AlB_2.

In situ measurements draw a detailed picture of the self-assembly process that we juxtapose with simulations to reveal the driving force behind the synthesis of BNSLs. The formation of AlB_2 and $NaZn_{13}$ BNSLs is frequently attributed to entropy[63,64] because of their high packing fractions[65,66] and because these are both equilibrium phases of the hard-sphere model,[67] whose phase behavior is solely dictated by entropy. However, we recently discovered that the self-assembly of the AlB_2 phase is kinetically prohibited in hard-sphere mixtures at a NC number ratio of 1:2,[68] indicating that more complex interactions are necessary for its formation.

The structure of the resulting BNSLs is largely determined by the effective interactions between NCs in solution. The NCs used in this work interact through solvent-mediated van der Waals interactions and superparamagnetic interactions in the case of Fe_3O_4 NCs.[69] Although many studies assume purely repulsive interactions in rationalizing observed phases in BNSLs (as mentioned above), the fact that our experiments find AlB_2, yet AlB_2 does not form from purely repulsive NCs at the number ratio 1:2 used in the experiments, implies attraction cannot be neglected.[68] Examples of NC interaction potentials with a repulsive core and attractive well have been obtained from atomistic simulations and theoretical models of similar spheroidal NCs, but the specific shape of the interaction potential varies among systems.[70-75] We choose to model NC interactions with a Mie potential,[76] which has a repulsive core and an attractive well whose depth and width control

the strength and range of attraction, respectively. To parameterize the potential, we consider the Noro-Frenkel law of corresponding states,[77] which dictates that only attractive wells with widths above a certain size will have stable liquid phases in their phase diagram. To compare cases with and without stable liquid phases, we examine two different well widths, described as "narrow well" and "wide well", with widths less than and greater than that size, respectively. We show the narrow and wide well in Figure 3a-b, scaling the range of the interaction between two NCs by the average of their effective sizes to account for size differences. For simplicity, the well depth, ε, is set equal for all interspecies interactions, *i.e.* $\varepsilon_{LL} = \varepsilon_{LS} = \varepsilon_{SS} = \varepsilon$. While this is an approximation, large differences in well depths frequently result in demixing,[78] which has been reported for other experiments on binary nanocrystal self-assembly but not those conducted here. Later, we discuss the plausible case of $\varepsilon_{LL} > \varepsilon_{LS} > \varepsilon_{SS}$, finding similar results to the case of equal attraction strength. We also examined a case in which the attractive well between the smaller NCs was significantly narrower than between large NCs, again finding a similar result; see Figure S16.

We note that our model assumes that more complex interactions, like many-body or anisotropic effects, either do not play a large role in determining the phase behavior of these NCs or they conspire to produce an effective interaction similar to the model. If we detect in simulation the phases observed in experiment while neglecting these more complex interactions, we can then infer that the simpler interactions are likely responsible for the formation of these phases. Furthermore, more complex interactions such as dipolar interactions[79,80] are more likely to be influenced by the specifics of the NC and solvent compositions, but the AlB_2 and $NaZn_{13}$ phases have been reported for many NC and solvent compositions,[21,22,63,78-82] reducing the likelihood that composition-dependent interactions are necessary for their self-assembly.

To reveal how the range and strength of interaction affect thermodynamic phase behavior, we compute phase diagrams for a NC number ratio of 1:2, as shown in Figure 3c-d. In the presence of the narrow well, the gas and solid AlB_2 phases are both stable. In contrast, in the presence of the wide well a region of vapor-liquid coexistence is stable above a critical well-depth ε_c; see Figures 3d and S17. This is consistent with the aforementioned Noro-Frenkel law of corresponding states,[77] which predicts that wider potential wells exhibit a stable liquid–gas transition.

While these phase diagrams show the equilibrium predictions for a given set of parameters, they do not indicate whether a phase is kinetically accessible. To study whether the AlB_2 phase will form, we slowly compress an initially disordered fluid under periodic boundary conditions. A combination of Steinhardt order parameters enables the quantification of the fraction of larger NCs that become crystalline as a function of time, N_{AlB_2}/N_{Total}; see Figure S18 for calculation details.[83] When using a narrow well at least 1.0 kT deep, over 50% of larger NCs crystallize by the end of the simulations, as shown in Figure 3e. There is limited crystallization for a shallower well of 0.5 kT, and no crystallization when the NCs are purely repulsive. In contrast, only minimal crystallization occurs with the wide well, with at most 6% of larger NCs registering as crystalline even for the deepest well investigated, 2.5 kT, as shown in Figure 3f.

These results show that a deep, narrow attractive well substantially improves the crystallization kinetics of AlB_2. A similar kinetic enhancement has been reported in simulations of single-component systems (as discussed below), but to our knowledge this is the first demonstration of such an effect in a multicomponent system of this nature. Furthermore, the effect is more dramatic for the case of AlB_2, because AlB_2 fails to crystallize at all without an attractive well but crystallizes readily with one. In comparable single-component systems, a narrow attractive well

can improve crystallization kinetics, but self-assembly still occurs readily without one (i.e. when the NCs resemble hard spheres).

We can rationalize this improvement to kinetics by considering the phase diagrams shown in Figures 3c-d. In general, crystal nucleation and growth is strongly influenced by the degree of supersaturation and particle mobility. In the phase diagram shown in Figure 3c, the solid become stable at low densities (where the particles are highly mobile) for a narrow, deep attractive well. A similar stabilization of the solid phase occurs for the wide well system, but the dense liquid phase is also stabilized, reducing the supersaturation. We quantify these effects by computing the chemical potential driving force between the crystal and fluid phases as a function of NC mobility in Figure S19, finding that deep, narrow wells do result in higher chemical potential driving forces at higher particle diffusivities. We also note that this principle of achieving high driving forces at low density is similar to that proposed for colloids with small attractive patches.[84]

To place these observations in a more general context, we investigated the crystallization of two related systems: a single-component face-centered cubic crystal (FCC) and the two-component $NaZn_{13}$ crystal for the narrow well at different well depths. In Figure S20, we show that, as with AlB_2, crystallization of both structures occurs at increasingly lower densities, although for FCC this shift is not too important because self-assembly still occurs readily without an attractive well. Furthermore, above its critical well depth, we find that AlB_2 crystallized through a two-step process in which a dense liquid forms first; see Figures S21 and S22. This switch to a two-step nucleation process at the critical point is consistent with previous reports for single-component systems. Thus, we conclude that crystallization in our binary systems occurs very similarly to that in single-component systems, except that an attractive force is required to observe the formation of some binary crystals.

In summary, our results indicate that the interaction between NCs during self-assembly is consistent with a pair potential characterized by a narrow well. We note that such a pair potential is fairly common for colloids in which vdW forces are the largest contribution to inter-NC attraction. Furthermore, we note that the narrow attractive well we use closely resembles that used for similar NCs in a recent study in which the attraction between NCs was assumed to be entirely vdW interactions between NC cores.[29] We also note that AlB_2 will self-assemble for a broad range of well depths greater than 0.5 kT, which possibly explains why it self-assembles for a NCs with different compositions, including the CdO NCs used here.

We next checked for further consistency with experiment by simulating conditions closer to experiment by adding NC polydispersity and spherical confinement to the simulations. We determine the polydispersity of each NC species by SAXS, Figure S1, and simulate the interaction of each NC with the confining boundary of the droplet using a Weeks-Chandler-Anderson potential.[85] Unsurprisingly, we found that adding polydispersity disfavored crystallization, but that crystallization was still possible on our time scales for the highest well depth examined in Figure 3 (2.5 kT), so we used that well depth in these simulations. Each simulation system is initialized as a colloidal fluid in a droplet, then slowly compressed to induce self-assembly. In close agreement with experiment, AlB_2 forms at a NC number ratio of 1:2, while $NaZn_{13}$ forms at 1:13. Interestingly, crystallization begins at a slightly lower volume fraction for $NaZn_{13}$ than AlB_2, 0.528 and 0.572 respectively, as shown in Figure 4a. Simulations performed at lower volume fractions did not result in self-assembly. As shown by the kinetic change in the fraction of crystalline particles, rapid crystal growth follows nucleation. Consistent with experiments, we find no intermediate phases that precede the final phases, indicating classical nucleation from a dense fluid

phase.[30,31] Furthermore, we conclude that spherical confinement does not influence the identity of the self-assembled structure in the systems investigated here.

Simulations provide the unparalleled advantage of directly visualizing crystal nucleation,[86-88] a process notoriously elusive to capture in experiments. The early stages of assembly for $NaZn_{13}$ and AlB_2 BNSLs are shown in Figures 4b and 4c, respectively. To highlight the crystalline nuclei, we color only the NCs identified as being in a crystalline environment, while fluid-like NCs are shown as smaller grey spheres. For both $NaZn_{13}$ and AlB_2 BNSLs, the critical nuclei emerge from the fluid multiple particle diameters away from the surface of the droplet, allowing us to conclude that these BNSLs undergo homogeneous nucleation. Only after nucleation do the crystallites of $NaZn_{13}$ and AlB_2 BNSL spread to the wall. This behavior is unaffected by the size of the droplet, as shown by replacing the spherical walls with flat walls to simulate significantly larger droplets, as shown in Figure S23. We find no evidence for exotic pre-nucleation clusters.[63,89]

The final stages of growth result in the crystals shown in Figures 4d-e. The $NaZn_{13}$ grains are easily identifiable by the simple cubic arrangement of the larger NCs. A single crystal grain spans most of the spherical superstructure, consistent with the experimental results shown in Figure 2. In contrast, multiple grains of AlB_2 are present. This qualitatively agrees with the SAXS measurements showing smaller grains for AlB_2 than $NaZn_{13}$, although specific crystal grains are harder to visualize in the TEM micrographs, making a quantitative comparison between simulation and experiment challenging.

An apparent discrepancy remains between experiment and simulation: experimental results indicate the presence of ~20% AlB_2 as a second phase for samples prepared at a NC number ratio

of 1:13, while simulations show less than 1% AlB_2. Interestingly, reducing the magnitude of the attraction between smaller NCs results in the coexistence of AlB_2 and $NaZn_{13}$ at a NC number ratio of 1:13, removing the discrepancy as shown in Figure S24. This adjustment is consistent with the dependence of van der Waals and superparamagnetic interactions on NC size.[90]

Conclusions.

We show a remarkable correspondence between experiment and simulation on the synthesis of BNSLs through self-assembly. While early efforts using evaporation-driven self-assembly have revealed the tendency to nucleate multiple polymorphs simultaneously,[22,79,91-93] our results show that emulsion-templated assembly provides a more controlled pathway towards the generation of phase-pure BNSLs. Under spherical confinement, NCs readily nucleate into binary phases isostructural to AlB_2 and $NaZn_{13}$ without intermediate liquid or crystal phases. The burst of crystal nucleation is followed by a gradual lattice contraction to result in multifunctional, 3D, dense, crystalline binary phases. We can accurately reproduce these experimental results in simulation by introducing a short-ranged, attractive potential which kinetically promotes self-assembly. This direct link between experiments and simulations reveals that BNSLs nucleate homogeneously and directly, without intermediate solid phases preceding the final crystal. Aspects of our results likely apply to NCs coated with DNA-based ligands,[40,94-96] which may provide more continuous control over the range of interactions and thus allow for a more direct probing of the remaining open questions. In achieving a closer correspondence between experiment and simulation, and demonstrating the importance of short-range attraction for assembly kinetics, this work represents a crucial first step in *a priori* prediction of BNSLs towards the deterministic hetero-integration of NCs into multifunctional structures, targeting applications in photonics,[53,58-60,97-99] excitonics,[58,100] phononics,[101,102] and catalysis.[103,104]

Methodology

Experiments

Synthesis and characterization of the NC building blocks: Oleate-functionalized PbS (lead sulfide, rock-salt structure, 4.5 ± 0.4 nm and 6.4 ± 0.6 nm in diameter), Fe_3O_4 (iron oxide, cubic spinel structure, 10.4 ± 0.6 nm in diameter), and FICO (fluorine and indium co-doped cadmium oxide, rock-salt structure, 13.2 ± 0.9 nm in diameter) NCs were synthesized by following reported procedures and redispersed in toluene.[103,105,106] The NC concentration was determined either by spectrophotometry by using a published sizing curve[107] (PbS, Figure S3) or by weighing the dry pellet (Fe_3O_4 and FICO). The size of the inorganic cores of the NCs was determined by fitting the SAXS pattern measured from a dilute dispersion of NCs with a spherical form factor, Figure S1. The form factor was convoluted with a Gaussian distribution of sizes to account for NC polydispersity. The fitting was performed by using the free software SASfit.[108] The effective size of the NCs was determined by imaging a monolayer of NCs by TEM, calculating the fast-Fourier transform of the image, and extracting the center-to-center distance between nearest neighbors, Figure S2. A complete description of these procedures is available in the supplementary information.

***In situ* SAXS**: The kinetic patterns were collected at the SMI beamline, Brookhaven National Laboratory, using a recently developed experimental setup.[28] To conserve beamtime, we expanded the setup to support the simultaneous measurement of 4 samples by translating the sample stage vertically; see schematic in Figure S4. Each sample was prepared as follows: A 20 mL scintillation vial was charged with 8 mL of 200 mM sodium dodecyl sulfate in water. Subsequently, the vial was charged with 2 mL of a NC dispersion in 22 v/v % toluene and 78 v/v % hexanes with a total

NC volume fraction of 0.001. The vial was capped and vigorously vortexed for 60 seconds using a vortex mixer (Fisher) to generate the emulsion. The emulsion was then uncapped and diluted by adding 10 mL of 200 mM sodium dodecyl sulfate in water. A 1-inch octagonal stir bar was then added to the diluted emulsion. The vial was placed on a hotplate (IKA plate) equipped with a thermocouple and a heating block for vials, heated to 70 °C while stirring at 500 rpm, and allowed to flow by means of a peristaltic pump (Cole-Palmer) at a flow rate of 10 mL/minute through a closed loop of Viton peristaltic tubing (Cole-Palmer). The closed loop included a custom-made flow cell consisting of a 1 mm quartz capillary tube (Charles Supper). The X-ray beam was aligned with the center of the capillary. This setup allowed us to measure the scattering pattern from the emulsion as evaporation occurred from the uncapped vial. The integration time for each measurement was set to 1 second, the time between consecutive acquisitions was 28 seconds, the beam energy was 16.1 keV, and the sample to detector distance was 6.3 meters. The q-range was calibrated against a silver behenate standard. The two-dimensional patterns were azimuthally averaged, and background subtracted to yield $I(q,t)$, where t is the time. The kinetic structure factor, $S(q,t)$, was then obtained by calculating $S(q,t) = I(q,t)/I(q,0)$ since at the beginning of the experiment the NCs are well dispersed within the droplets.

Structural parameters of AlB_2: For a hexagonal structure (Figure S5), the expected reflections q_{hkl} for the planes of indexes hkl are:

$$q_{hkl} = \sqrt{\frac{4}{3}\frac{h^2 + hk + k^2}{a^2} + \frac{l^2}{c^2}}$$

We first extracted the c/a factor for the AlB_2 structure for the last data point, $t = t_{end}$. We did so empirically by generating the expected positions q_{hkl} of the reflections for a given value of c/a,

and comparing with the experimental results until an agreement was found. We found that the value of c/a does not vary as the structure evolves during drying. To calculate the kinetic structural parameters, we first fitted each $S(q,t)$ curve with a superposition of Lorentzian curves with line shape:

$$L(q) = \frac{Aw^2}{(q - q_{hkl})^2 + w^2}$$

centered around the expected q_{hkl} positions, with amplitude A and full width at half maximum $2w$. Since q_{101} was the most isolated reflection, we used it to calculate the kinetic structural parameters. From the Scherrer equation, we calculated the average crystal size as $\xi = 2\pi K/2w = \pi K/w$, where $K = 1.0747$ is the Scherrer constant used for a spherical crystal.[109] The lattice parameter, also equal to the center-to-center distance, or bond length, between larger (L) NCs was calculated as:

$$b_{LL} = a = \frac{2\pi}{q_{101}}\sqrt{\frac{4}{3} + \frac{1}{(c/a)^2}}$$

The surface-to-surface distance between larger NCs was then calculated as $d_{LL} = b_{LL} - \sigma_L$, where σ_L is the average diameter of the inorganic cores of the larger NCs as measured by *ex situ* SAXS. The bond length between smaller (S) NCs was calculated by scaling by the expected values for the bond lengths in the atomic AlB_2 structure for which $b_{LL,At} = 0.30090\,nm$ and $b_{SS,At} = 0.17372\,nm$ so that $b_{SS} = b_{LL}(b_{SS,At}/b_{LL,At})$. The surface-to-surface distance between smaller NCs was then calculated as $d_{SS} = b_{SS} - \sigma_S$, where σ_S is the average diameter of the inorganic cores of the smaller NCs as measured by *ex situ* SAXS. The bond length between larger and smaller NCs was then calculated as $b_{LS} = b_{LL}(b_{LS,At}/b_{LL,At})$, where $b_{LS,At}$ is the bond length in the atomic

AlB_2 structure for measured value of c/a in the nanocrystal superstructure. For $c/a = 0.99$, $b_{AB,At} = 0.22883\ nm$. The surface-to-surface distance between larger and smaller NCs was then determined as $d_{LS} = b_{LS} - \sigma_L/2 - \sigma_S/2$. Additional details are provided in the supporting information.

Structural parameters of $NaZn_{13}$: For a cubic structure (Figure S13), the expected reflections q_{hkl} for the planes of indexes hkl are:

$$q_{hkl} = \frac{2\pi}{a}\sqrt{\mathrm{h}^2 + \mathrm{k}^2 + \mathrm{l}^2}$$

To calculate the kinetic structural parameters, we first fitted each $S(q,t)$ curve with a superposition of Lorentzian curves with line shape centered around the expected q_{hkl} positions, with amplitude A and full width at half maximum $2w$. Since q_{200} was the most isolated reflection, we used it to calculate the kinetic structural parameters. From the Scherrer equation, we calculated the average crystal size as $\xi = \pi K/w$. The lattice parameter a, twice the center-to-center distance, or bond length, between larger NCs, b_{LL}, was calculated as $2b_{LL} = a = 4\pi/q_{200}$. The surface-to-surface distance between larger NCs was then calculated as $d_{LL} = b_{LL} - \sigma_L$. The bond length between smaller NCs was calculated by scaling by the expected values for the bond lengths in the atomic $NaZn_{13}$ structure for which $b_{LL,At} = 0.61365\ nm$ and $b_{SS,At} = 0.25664\ nm$ so that $b_{SS} = b_{LL}(b_{SS,At}/b_{LL,At})$. The surface-to-surface distance between smaller NCs was then calculated as $d_{SS} = b_{SS} - \sigma_S$. The bond length between larger and smaller NCs was then calculated as $b_{LS} = b_{LL}(b_{LS,At}/b_{LL,At})$ where $b_{LS,At} = 0.35647\ nm$ is the bond length in the atomic $NaZn_{13}$ structure. The surface-to-surface distance between larger and smaller NCs was then determined as $d_{LS} = b_{LS} - \sigma_L/2 - \sigma_S/2$. Additional details are provided in the supporting information.

Electron microscopy: For TEM and STEM imaging, a JEOL F200 microscope was operated at 200 kV. During imaging, magnification, focus and tilt angle were varied to yield information about the crystal structure and super structure of the particle systems. To prepare the superstructures for imaging, after the emulsion had fully dried, the binary NC superstructures were washed twice in a solution of 20 mM sodium dodecyl sulfate in water by centrifugation at 3000 g for 30 minutes, and redispersed. 10 μL of the dispersion was drop casted on a carbon-coated TEM grid (EMS) and dried under vacuum for 1 hour. The grid was then dipped in a cleaning solution consisting of 1:2 water:isopropranol by volume, and dried for 1 hour under vacuum.

Rendering: The coordinates for a three-dimensional superlattice with parameters matching experiment were initially generated by using a self-developed script. A sphere of a desired size matching a superstructure was then carved from the superlattice. The positions and sizes of all particles were then sent to the free software Blender 2.93 and rendered.

Simulations

We used molecular dynamics (MD) with the HOOMD-Blue simulation toolkit[110] to simulate a binary mixture of NCs with interactions modeled by the Mie (IPL) potential:

$$U_{ij}(r_{ij}) = \varepsilon_{ij}\left(\frac{n}{n-m}\right)\left(\frac{n}{m}\right)^{\frac{m}{n-m}}\left(\left(\frac{\sigma_{ij}}{r_{ij}}\right)^{n} - \left(\frac{\sigma_{ij}}{r_{ij}}\right)^{m}\right)$$

where $U_{ij}(r_{ij})$ is the energy between two NCs (particles) *i* and *j* separated by a distance r_{ij}. The potential is described by four parameters: a measure of the particle's size, σ_{ij}; the power of the repulsive component, *n*; the magnitude of the interaction, ε_{ij}; and the length scale of the attractive interaction, *m*. We set σ_{ij} to match the effective size ratio of the NCs used in experiment: $\sigma_{SS} =$

$0.55 * \sigma_{LL}$, $\sigma_{LS} = \frac{0.55+1}{2} * \sigma_{LL}$, and $\sigma_{LL} = 1$,where L represents the larger NCs and S the smaller NCs. For simplicity, we set the depth of the potential well to be equal for all particle pairs: $\varepsilon_{LL} = \varepsilon_{LS} = \varepsilon_{SS} = \varepsilon$. We also use σ to represent σ_{LL} in the text. For consistency with previous works,[68] we set the power n to a value of 50. We analyze systems with m of 6 and 25, which we refer to as "wide well" and "narrow well" respectively. The resulting potentials are shown in Figure 3a-b for a well-depth of 1.0 kT. Throughout the paper we manipulate the well depth by changing the temperature, which is inversely proportional to the well depth. We define the units of time as $\tau = \sigma \left(\frac{w}{\varepsilon}\right)^{\frac{1}{2}}$, where w is mass and set to 1 for every type of particle. For $\varepsilon/kT = 0$ shown in Figure 3c-d, we simulated an inverse power law potential at 1.0 kT, similarly to previous work.[68]

To compute the free energies of different phases in Figure 3c and 3d, we combined thermodynamic integration with the Einstein molecule method,[111] a variant of the Frenkel-Ladd method,[112] using at least 2,000 particles in every case. The free energies of the gas and liquid phases were computed at a stoichiometry of 1:2. Self-assembly was attempted with 27,000 particles by slowly compressing the particles from an initially disordered fluid state to a crystalline or kinetically arrested amorphous state. In Figure S25 we give the range of densities compressed over for each well depth and width. We also compute the diffusion coefficient in the vicinity of kinetic arrest. We used NVT simulations based on the MTK equations[113] to thermostat our simulations in Figure 3e-f and NVT simulations using a Langevin integrator[114] to thermostat our simulations in Figure 4.

For the simulations in Figure 4, we treat the distribution of particle sizes as a mixture of two normal distributions: one centered at a size of $1\sigma_{LL}$ and one centered at a size of $0.55\sigma_{LL}$. The standard deviations (s) of the normal distributions were chosen to match experiment: $s = 0.047\sigma_{LL}$ for that

of the larger particles and $s = 0.063\sigma_{ss}$ for that of the smaller particles. We then discretized the distributions, with 13 bins associated with each peak. We placed the particles inside a spherical droplet, whose edges repel the particles with a Weeks-Chandler-Anderson potential.[85] We computed an effective packing fraction by calculating an effective particle size according to the prescription of Barker and Henderson.[115] We scaled the wall's range of interaction by $\sigma_i/2$, which accounts for the different sizes of the particles.

We used Steinhardt order parameters[83] in Figures 3 and 4 to identify crystalline particles. The specific combinations for each crystal are shown in Figure S18. The parameters were calculated using the *freud* software library.[116] In Figure S22 we used the local density of each particle to infer the occurrence of two-step nucleation. We computed the local density using the implementation provided by *freud*[116], in which the contribution of each neighbor is scaled by the interparticle distance and diameter of the particle. We used $r_{max} = 1.3\sigma$ and a diameter of 1.0σ in the calculation. We classified particles as locally dense if the local density was greater than $1.05/\sigma^3$, $1.6/\sigma^3$, and $2.5/\sigma^3$ for simulations of FCC, AlB_2, and $NaZn_{13}$, respectively. These cutoffs were chosen to separate particles belonging to the initial low-density fluid phase from denser fluid and crystal phases.

We used Ovito[117] to visualize our simulations throughout this work.

The computational workflow and data management for this publication was primarily supported by the *signac* data management framework.[118,119]

DATA AVAILABILITY

The authors declare that the data supporting the findings of this study are available within the article and its supplementary information files. Source data for the figures in the main text are available as supporting information.

CODE AVAILABILITY

Source code for HOOMD-blue is available at https://github.com/glotzerlab/hoomd-blue. Source data for the figures in the main text are available as supporting information. Sample codes are available as supporting information.

ACKNOWLEDGMENT

The authors acknowledge primary support from the National Science Foundation under Grant DMR-2019444. E.M. and S.Y. acknowledge support from the Office of Naval Research Multidisciplinary University Research Initiative Award ONR N00014-18-1-2497 for sample preparation and characterization. E.M. is grateful to the National Recovery and Resilience Plan (NRRP) PNR 2021-2022 (CUP B79J21038330001) for funding his position at Unipa. E.M. acknowledges the Fondo Finalizzato Alla Ricerca Di Ateneo (FFR) 2022-2023 of Unipa for funding. A.W.K. and C.R.K. acknowledge support from the Semiconductor Research Corporation (SRC) under the Nanomanufacturing Materials and Processes (NMP) trust via Task 2797.001. D.J.R. acknowledges support from the VIEST fellowship. G.G. acknowledges Solvay for financial support. C.B.M. acknowledges the Richard Perry University Professorship at the University of Pennsylvania. Support for the Dual Source and Environmental X-ray Scattering Facility at the University of Pennsylvania was provided by the Laboratory for Research on the Structure of Matter which is funded in part by NSF MRSEC 1720530. This research used resources of the

Center for Functional Nanomaterials and the National Synchrotron Light Source II, which are U.S. DOE Office of Science Facilities, at Brookhaven National Laboratory under Contract No. DESC0012704. Computational work used resources form the Extreme Science and Engineering Discovery Environment (XSEDE),[120] which is supported by National Science Foundation grant number ACI-1548562; XSEDE Award DMR 140129. Additional computational resources and services supported by Advanced Research Computing at the University of Michigan, Ann Arbor.

AUTHOR INFORMATION

Corresponding Author

*email: cbmurray@sas.upenn.edu, sglotzer@umich.edu

Author Contributions

E.M. designed the experiment. E.M., S.v.D., A.W.K., and D.A. synthesized and characterized the NC building blocks. E.M., S.v.D., S.Y., D.J.R., and E.H.R.T. measured the *in situ* scattering data. E.M. analyzed the results. E.H.R.T. provided local support at the beamline. E.M., G.G., and S.v.D. performed the electron microscopy studies. D.J.R. performed the magnetic measurements. R.A.L. and T.C.M. performed the simulations and analyzed the results. S.C.G. and C.B.M. supervised the project. The manuscript was written through contributions of all authors. All authors have given approval to the final version of the manuscript. ‡These authors contributed equally.

COMPETING INTERESTS

The authors declare no competing interests.

FIGURE CAPTIONS

Figure 1: Formation of colloidal AlB_2 binary nanocrystal superlattices (BNSLs). (a) Kinetic structure factor, S(q), of a binary dispersion of PbS and Fe_3O_4 nanocrystals (NCs) under spherical confinement of a drying emulsion. (b) S(q) patterns showing the emergence and evolution of diffraction peaks around the time of BNSL nucleation. (c) Final S(q) pattern identifying the BNSL structure as AlB_2. (d) Evolution of the crystalline lattice after nucleation, highlighting the kinetics of surface-to-surface distance between larger (L) and smaller (S) NCs, d (top), and average crystal size, ξ (bottom). The proposed assembly mechanism is shown as inset. (e) Transmission electron micrograph of PbS and Fe_3O_4 NCs crystallized into a three-dimensional AlB_2 BNSL. The fast-Fourier transform is shown as inset. (f) Model of the AlB_2 BNSL shown in (e).

Figure 2: Formation of colloidal $NaZn_{13}$ binary nanocrystal superlattices (BNSLs). (a) Kinetic structure factor, S(q), of a binary dispersion of PbS and FICO nanocrystals (NCs) under spherical confinement of a drying emulsion. (b) S(q) patterns showing the emergence and evolution of diffraction peaks around the time of BNSL nucleation. (c) Final S(q) pattern identifying the BNSL structure as $NaZn_{13}$ with a minority AlB_2 phase. (d) Evolution of the surface-to-surface distance between larger (L) and smaller (S) NCs, d (top), average crystal size, ξ (middle), and phase fraction (bottom) of the two binary phases during lattice compression. (e) Dark-field scanning transmission electron micrograph of a single-crystal $NaZn_{13}$ BNSL, and (f) its structural model. (g) Dark-field scanning transmission electron micrograph of a heterostructure showing the coexistence of $NaZn_{13}$ with a secondary phase.

Figure 3: The influence of attractive forces in binary mixtures. (a-b) Mie pair potentials shown as a function of the normalized interparticle distance, $U(r/\sigma)$, calculated for a well depth of 1 kT and for length scale parameters m = 25 (a) and m = 6 (b). The potential in (a) is described as the "narrow well" and the one in (b) as the "wide well" in the main text. For each potential, three types of interactions are shown: between larger (LL) nanocrystals (NCs), between larger and smaller (LS) NCs, and between smaller (SS) NCs. (c-d) Thermodynamic phase diagrams computed from free energy calculations for the narrow (c) and wide well (d) as a function of well depth, ε, and normalized particle density, $\rho\sigma^3$. The blue and orange lines demarcate the regions of gas-solid coexistence and vapor-liquid coexistence, respectively. Errors in the phase boundaries are smaller than the points. The dashed red line in (d) indicates the critical well depth ε_c above which vapor-liquid coexistence occurs. The phase diagrams are computed at a NC number ratio of 1:2. (e-f) The evolution of the number of AlB_2-like particles in self-assembly simulations through slow compression for the narrow (e) and wide well (f).

Figure 4: The self-assembly of AlB_2 and $NaZn_{13}$ in spherical droplets. In (a) we show the results of attempts to self-assemble AlB_2 and $NaZn_{13}$ with the deepest (2.5 kT), narrow well used in Figure 3. The curve labelled "$NaZn_{13}$" was obtained at a stoichiometry of 1:13, while the curve labelled "AlB_2" was obtained at a stoichiometry of 1:2; N_{crys}/N_{total} is the fraction of large particles we identify as $NaZn_{13}$-like or AlB_2-like respectively. In (b) and (c) we show early stages of the growing $NaZn_{13}$ and AlB_2 crystals, respectively. We show two different time points, (i) and (ii); the color of the images' borders match that of the corresponding timepoints in (a) from which they were taken. We show large particles identified as crystalline in blue and small particles neighboring a crystalline large particle in pink; all other particles are reduced in size and colored

grey. In (d) and (e), we visualize an inner slice of each droplet at the final time point of our simulations, coloring every particle. Unlike the simulations in Figure 3, each species is set to have the polydispersity of the corresponding experimental nanoparticles.

REFERENCES

1 Konstantatos, G. *et al.* Ultrasensitive solution-cast quantum dot photodetectors. *Nature* **442**, 180-183, doi:10.1038/nature04855 (2006).

2 Tang, X., Ackerman, M. M., Chen, M. & Guyot-Sionnest, P. Dual-band infrared imaging using stacked colloidal quantum dot photodiodes. *Nature Photonics* **13**, 277-282, doi:10.1038/s41566-019-0362-1 (2019).

3 Caruge, J. M., Halpert, J. E., Wood, V., Bulović, V. & Bawendi, M. G. Colloidal quantum-dot light-emitting diodes with metal-oxide charge transport layers. *Nature Photonics* **2**, 247-250, doi:10.1038/nphoton.2008.34 (2008).

4 Kim, T. *et al.* Efficient and stable blue quantum dot light-emitting diode. *Nature* **586**, 385-389, doi:10.1038/s41586-020-2791-x (2020).

5 Talapin, D. V. & Murray, C. B. PbSe Nanocrystal Solids for n- and p-Channel Thin Film Field-Effect Transistors. *Science* **310**, 86, doi:10.1126/science.1116703 (2005).

6 Zhao, Q. *et al.* Enhanced Carrier Transport in Strongly Coupled, Epitaxially Fused CdSe Nanocrystal Solids. *Nano Letters* **21**, 3318-3324, doi:10.1021/acs.nanolett.1c00860 (2021).

7 Luther, J. M. *et al.* Schottky Solar Cells Based on Colloidal Nanocrystal Films. *Nano Letters* **8**, 3488-3492, doi:10.1021/nl802476m (2008).

8 Swarnkar, A. *et al.* Quantum dot–induced phase stabilization of α-CsPbI3 perovskite for high-efficiency photovoltaics. *Science* **354**, 92-95, doi:10.1126/science.aag2700 (2016).

9 Lan, X. *et al.* Quantum dot solids showing state-resolved band-like transport. *Nature Materials* **19**, 323-329, doi:10.1038/s41563-019-0582-2 (2020).

10 Mueller, N. S. *et al.* Deep strong light–matter coupling in plasmonic nanoparticle crystals. *Nature* **583**, 780-784, doi:10.1038/s41586-020-2508-1 (2020).

11 Cherniukh, I. *et al.* Perovskite-type superlattices from lead halide perovskite nanocubes. *Nature* **593**, 535-542, doi:10.1038/s41586-021-03492-5 (2021).

12 Urban, J. J., Talapin, D. V., Shevchenko, E. V., Kagan, C. R. & Murray, C. B. Synergism in binary nanocrystal superlattices leads to enhanced p-type conductivity in self-assembled PbTe/Ag_2Te thin films. *Nature Materials* **6**, 115-121, doi:10.1038/nmat1826 (2007).

13 Chen, J. *et al.* Collective Dipolar Interactions in Self-Assembled Magnetic Binary Nanocrystal Superlattice Membranes. *Nano Letters* **10**, 5103-5108, doi:10.1021/nl103568q (2010).

14 Chen, J. *et al.* Bistable Magnetoresistance Switching in Exchange-Coupled CoFe2O4–Fe3O4 Binary Nanocrystal Superlattices by Self-Assembly and Thermal Annealing. *ACS Nano* **7**, 1478-1486, doi:10.1021/nn3052617 (2013).
15 Dong, A., Chen, J., Ye, X., Kikkawa, J. M. & Murray, C. B. Enhanced Thermal Stability and Magnetic Properties in NaCl-Type FePt–MnO Binary Nanocrystal Superlattices. *Journal of the American Chemical Society* **133**, 13296-13299, doi:10.1021/ja2057314 (2011).
16 Kang, Y. *et al.* Design of Pt–Pd Binary Superlattices Exploiting Shape Effects and Synergistic Effects for Oxygen Reduction Reactions. *Journal of the American Chemical Society* **135**, 42-45, doi:10.1021/ja3097527 (2013).
17 Kang, Y. *et al.* Engineering Catalytic Contacts and Thermal Stability: Gold/Iron Oxide Binary Nanocrystal Superlattices for CO Oxidation. *Journal of the American Chemical Society* **135**, 1499-1505, doi:10.1021/ja310427u (2013).
18 Zhang, M. *et al.* High-strength magnetically switchable plasmonic nanorods assembled from a binary nanocrystal mixture. *Nature Nanotechnology* **12**, 228-232, doi:10.1038/nnano.2016.235 (2017).
19 Cargnello, M. *et al.* Substitutional doping in nanocrystal superlattices. *Nature* **524**, 450-453, doi:10.1038/nature14872 (2015).
20 Lee, J.-S., Kovalenko, M. V., Huang, J., Chung, D. S. & Talapin, D. V. Band-like transport, high electron mobility and high photoconductivity in all-inorganic nanocrystal arrays. *Nature Nanotechnology* **6**, 348-352, doi:10.1038/nnano.2011.46 (2011).
21 Redl, F. X., Cho, K. S., Murray, C. B. & O'Brien, S. Three-dimensional binary superlattices of magnetic nanocrystals and semiconductor quantum dots. *Nature* **423**, 968-971, doi:10.1038/nature01702 (2003).
22 Shevchenko, E. V., Talapin, D. V., Kotov, N. A., O'Brien, S. & Murray, C. B. Structural diversity in binary nanoparticle superlattices. *Nature* **439**, 55-59, doi:10.1038/nature04414 (2006).
23 Kiely, C. J., Fink, J., Brust, M., Bethell, D. & Schiffrin, D. J. Spontaneous ordering of bimodal ensembles of nanoscopic gold clusters. *Nature* **396**, 444-446, doi:10.1038/24808 (1998).
24 Heil, C. M. & Jayaraman, A. Computational Reverse-Engineering Analysis for Scattering Experiments of Assembled Binary Mixture of Nanoparticles. *ACS Materials Au* **1**, 140-156, doi:10.1021/acsmaterialsau.1c00015 (2021).
25 Bommineni, P. K., Klement, M. & Engel, M. Spontaneous Crystallization in Systems of Binary Hard Sphere Colloids. *Physical Review Letters* **124**, 218003, doi:10.1103/PhysRevLett.124.218003 (2020).
26 Wang, D. *et al.* Binary icosahedral clusters of hard spheres in spherical confinement. *Nature Physics* **17**, 128-134, doi:10.1038/s41567-020-1003-9 (2021).
27 Coli, G. M. & Dijkstra, M. An Artificial Neural Network Reveals the Nucleation Mechanism of a Binary Colloidal AB13 Crystal. *ACS Nano* **15**, 4335-4346, doi:10.1021/acsnano.0c07541 (2021).
28 Marino, E., Kodger, T. E., Wegdam, G. H. & Schall, P. Revealing Driving Forces in Quantum Dot Supercrystal Assembly. **30**, 1803433, doi:https://doi.org/10.1002/adma.201803433 (2018).

29 Montanarella, F. *et al.* Crystallization of Nanocrystals in Spherical Confinement Probed by in Situ X-ray Scattering. *Nano Letters* **18**, 3675-3681, doi:10.1021/acs.nanolett.8b00809 (2018).
30 Weidman, M. C., Smilgies, D.-M. & Tisdale, W. A. Kinetics of the self-assembly of nanocrystal superlattices measured by real-time in situ X-ray scattering. *Nature Materials* **15**, 775-781, doi:10.1038/nmat4600 (2016).
31 Geuchies, J. J. *et al.* In situ study of the formation mechanism of two-dimensional superlattices from PbSe nanocrystals. *Nature Materials* **15**, 1248-1254, doi:10.1038/nmat4746 (2016).
32 Abécassis, B., Testard, F. & Spalla, O. Gold Nanoparticle Superlattice Crystallization Probed In Situ. *Physical Review Letters* **100**, 115504, doi:10.1103/PhysRevLett.100.115504 (2008).
33 Narayanan, S., Wang, J. & Lin, X.-M. Dynamical Self-Assembly of Nanocrystal Superlattices during Colloidal Droplet Evaporation by in situ Small Angle X-Ray Scattering. *Physical Review Letters* **93**, 135503, doi:10.1103/PhysRevLett.93.135503 (2004).
34 Connolly, S., Fullam, S., Korgel, B. & Fitzmaurice, D. Time-Resolved Small-Angle X-ray Scattering Studies of Nanocrystal Superlattice Self-Assembly. *Journal of the American Chemical Society* **120**, 2969-2970, doi:10.1021/ja974273e (1998).
35 Yu, Y., Yu, D., Sadigh, B. & Orme, C. A. Space- and time-resolved small angle X-ray scattering to probe assembly of silver nanocrystal superlattices. *Nature Communications* **9**, 4211, doi:10.1038/s41467-018-06734-9 (2018).
36 Wu, L. *et al.* High-temperature crystallization of nanocrystals into three-dimensional superlattices. *Nature* **548**, 197-201, doi:10.1038/nature23308 (2017).
37 Gong, J. *et al.* Shape-dependent ordering of gold nanocrystals into large-scale superlattices. *Nature Communications* **8**, 14038, doi:10.1038/ncomms14038 (2017).
38 Lin, H. *et al.* Clathrate colloidal crystals. *Science* **355**, 931, doi:10.1126/science.aal3919 (2017).
39 Yue, K. *et al.* Geometry induced sequence of nanoscale Frank–Kasper and quasicrystal mesophases in giant surfactants. *Proceedings of the National Academy of Sciences* **113**, 14195, doi:10.1073/pnas.1609422113 (2016).
40 Macfarlane, R. J. *et al.* Nanoparticle Superlattice Engineering with DNA. *Science* **334**, 204, doi:10.1126/science.1210493 (2011).
41 Tang, Z., Zhang, Z., Wang, Y., Glotzer, S. C. & Kotov, N. A. Self-Assembly of CdTe Nanocrystals into Free-Floating Sheets. *Science* **314**, 274, doi:10.1126/science.1128045 (2006).
42 Leunissen, M. E. *et al.* Ionic colloidal crystals of oppositely charged particles. *Nature* **437**, 235-240, doi:10.1038/nature03946 (2005).
43 Wang, T. *et al.* Self-Assembled Colloidal Superparticles from Nanorods. *Science* **338**, 358-363, doi:10.1126/science.1224221 (2012).
44 Lu, C., Akey, A. J., Dahlman, C. J., Zhang, D. & Herman, I. P. Resolving the Growth of 3D Colloidal Nanoparticle Superlattices by Real-Time Small-Angle X-ray Scattering. *Journal of the American Chemical Society* **134**, 18732-18738, doi:10.1021/ja307848h (2012).

45 Rosen, D. J., Yang, S., Marino, E., Jiang, Z. & Murray, C. B. In Situ EXAFS-Based Nanothermometry of Heterodimer Nanocrystals under Induction Heating. *The Journal of Physical Chemistry C* **126**, 3623-3634, doi:10.1021/acs.jpcc.2c00608 (2022).
46 Rosen, D. J. *et al.* Microwave Heating of Nanocrystals for Rapid, Low-Aggregation Intermetallic Phase Transformations. *ACS Materials Letters* **4**, 823-830, doi:10.1021/acsmaterialslett.2c00174 (2022).
47 Yang, S. *et al.* Self-Assembly of Atomically Aligned Nanoparticle Superlattices from Pt–Fe3O4 Heterodimer Nanoparticles. *Journal of the American Chemical Society* **145**, 6280-6288, doi:10.1021/jacs.2c12993 (2023).
48 Gabbani, A. *et al.* Magnetoplasmonics beyond Metals: Ultrahigh Sensing Performance in Transparent Conductive Oxide Nanocrystals. *Nano Letters* **22**, 9036-9044, doi:10.1021/acs.nanolett.2c03383 (2022).
49 Velev Orlin, D., Lenhoff Abraham, M. & Kaler Eric, W. A Class of Microstructured Particles Through Colloidal Crystallization. *Science* **287**, 2240-2243, doi:10.1126/science.287.5461.2240 (2000).
50 Wang, P.-p., Qiao, Q., Zhu, Y. & Ouyang, M. Colloidal Binary Supracrystals with Tunable Structural Lattices. *Journal of the American Chemical Society* **140**, 9095-9098, doi:10.1021/jacs.8b05643 (2018).
51 Kister, T., Mravlak, M., Schilling, T. & Kraus, T. Pressure-controlled formation of crystalline, Janus, and core–shell supraparticles. *Nanoscale* **8**, 13377-13384, doi:10.1039/C6NR01940D (2016).
52 Abelson, A. *et al.* Collective topo-epitaxy in the self-assembly of a 3D quantum dot superlattice. *Nature Materials* **19**, 49-55, doi:10.1038/s41563-019-0485-2 (2020).
53 Marino, E. *et al.* Monodisperse Nanocrystal Superparticles through a Source–Sink Emulsion System. *Chemistry of Materials* **34**, 2779-2789, doi:10.1021/acs.chemmater.2c00039 (2022).
54 Lacava, J., Born, P. & Kraus, T. Nanoparticle Clusters with Lennard-Jones Geometries. *Nano Letters* **12**, 3279-3282, doi:10.1021/nl3013659 (2012).
55 de Nijs, B. *et al.* Entropy-driven formation of large icosahedral colloidal clusters by spherical confinement. *Nature Materials* **14**, 56-60, doi:10.1038/nmat4072 (2015).
56 Wintzheimer, S. *et al.* Supraparticles: Functionality from Uniform Structural Motifs. *ACS Nano* **12**, 5093-5120, doi:10.1021/acsnano.8b00873 (2018).
57 Marino, E. *et al.* Favoring the Growth of High-Quality, Three-Dimensional Supercrystals of Nanocrystals. *The Journal of Physical Chemistry C* **124**, 11256-11264, doi:10.1021/acs.jpcc.0c02805 (2020).
58 Marino, E. *et al.* Simultaneous Photonic and Excitonic Coupling in Spherical Quantum Dot Supercrystals. *ACS Nano* **14**, 13806-13815, doi:10.1021/acsnano.0c06188 (2020).
59 Savo, R. *et al.* Broadband Mie driven random quasi-phase-matching. *Nature Photonics* **14**, 740-747, doi:10.1038/s41566-020-00701-x (2020).
60 Montanarella, F. *et al.* Lasing Supraparticles Self-Assembled from Nanocrystals. *ACS Nano* **12**, 12788-12794, doi:10.1021/acsnano.8b07896 (2018).
61 Tang, Y. *et al.* Highly Stable Perovskite Supercrystals via Oil-in-Oil Templating. *Nano Letters* **20**, 5997-6004, doi:10.1021/acs.nanolett.0c02005 (2020).
62 Patterson, A. L. The Scherrer Formula for X-Ray Particle Size Determination. *Physical Review* **56**, 978-982, doi:10.1103/PhysRev.56.978 (1939).

63 Bodnarchuk, M. I., Kovalenko, M. V., Heiss, W. & Talapin, D. V. Energetic and Entropic Contributions to Self-Assembly of Binary Nanocrystal Superlattices: Temperature as the Structure-Directing Factor. *Journal of the American Chemical Society* **132**, 11967-11977, doi:10.1021/ja103083q (2010).
64 Yang, Z., Wei, J. & Pileni, M.-P. Metal–Metal Binary Nanoparticle Superlattices: A Case Study of Mixing Co and Ag Nanoparticles. *Chemistry of Materials* **27**, 2152-2157, doi:10.1021/acs.chemmater.5b00123 (2015).
65 Murray, M. J. & Sanders, J. V. Close-packed structures of spheres of two different sizes II. The packing densities of likely arrangements. *Philosophical Magazine A* **42**, 721-740, doi:10.1080/01418618008239380 (1980).
66 Chen, Z. & O'Brien, S. Structure Direction of II−VI Semiconductor Quantum Dot Binary Nanoparticle Superlattices by Tuning Radius Ratio. *ACS Nano* **2**, 1219-1229, doi:10.1021/nn800129s (2008).
67 Eldridge, M. D., Madden, P. A. & Frenkel, D. Entropy-driven formation of a superlattice in a hard-sphere binary mixture. *Nature* **365**, 35-37, doi:10.1038/365035a0 (1993).
68 LaCour, R. A., Moore, T. C. & Glotzer, S. C. Tuning Stoichiometry to Promote Formation of Binary Colloidal Superlattices. *Physical Review Letters* **128**, 188001, doi:10.1103/PhysRevLett.128.188001 (2022).
69 Bishop, K. J. M., Wilmer, C. E., Soh, S. & Grzybowski, B. A. Nanoscale Forces and Their Uses in Self-Assembly. *Small* **5**, 1600-1630, doi:https://doi.org/10.1002/smll.200900358 (2009).
70 Schapotschnikow, P., Pool, R. & Vlugt, T. J. H. Molecular Simulations of Interacting Nanocrystals. *Nano Letters* **8**, 2930-2934, doi:10.1021/nl8017862 (2008).
71 Liepold, C., Smith, A., Lin, B., de Pablo, J. & Rice, S. A. Pair and many-body interactions between ligated Au nanoparticles. *The Journal of Chemical Physics* **150**, 044904, doi:10.1063/1.5064545 (2019).
72 Baran, Ł. & Sokołowski, S. Effective interactions between a pair of particles modified with tethered chains. *The Journal of Chemical Physics* **147**, 044903, doi:10.1063/1.4994919 (2017).
73 Munaò, G., Correa, A., Pizzirusso, A. & Milano, G. On the calculation of the potential of mean force between atomistic nanoparticles. *The European Physical Journal E* **41**, 38, doi:10.1140/epje/i2018-11646-3 (2018).
74 Kaushik, A. P. & Clancy, P. Solvent-driven symmetry of self-assembled nanocrystal superlattices—A computational study. *Journal of Computational Chemistry* **34**, 523-532, doi:https://doi.org/10.1002/jcc.23152 (2013).
75 Kister, T., Monego, D., Mulvaney, P., Widmer-Cooper, A. & Kraus, T. Colloidal Stability of Apolar Nanoparticles: The Role of Particle Size and Ligand Shell Structure. *ACS Nano* **12**, 5969-5977, doi:10.1021/acsnano.8b02202 (2018).
76 Mie, G. Zur kinetischen Theorie der einatomigen Körper. *Annalen der Physik* **316**, 657-697, doi:https://doi.org/10.1002/andp.19033160802 (1903).
77 Noro, M. G. & Frenkel, D. Extended corresponding-states behavior for particles with variable range attractions. *The Journal of Chemical Physics* **113**, 2941-2944, doi:10.1063/1.1288684 (2000).
78 Coropceanu, I., Boles, M. A. & Talapin, D. V. Systematic Mapping of Binary Nanocrystal Superlattices: The Role of Topology in Phase Selection. *Journal of the American Chemical Society* **141**, 5728-5740, doi:10.1021/jacs.8b12539 (2019).

79 Shevchenko, E. V., Talapin, D. V., Murray, C. B. & O'Brien, S. Structural Characterization of Self-Assembled Multifunctional Binary Nanoparticle Superlattices. *Journal of the American Chemical Society* **128**, 3620-3637, doi:10.1021/ja0564261 (2006).
80 Yang, Z., Wei, J., Bonville, P. & Pileni, M.-P. Beyond Entropy: Magnetic Forces Induce Formation of Quasicrystalline Structure in Binary Nanocrystal Superlattices. *Journal of the American Chemical Society* **137**, 4487-4493, doi:10.1021/jacs.5b00332 (2015).
81 Evers, W. H. *et al.* Entropy-Driven Formation of Binary Semiconductor-Nanocrystal Superlattices. *Nano Letters* **10**, 4235-4241, doi:10.1021/nl102705p (2010).
82 Boles, M. A. & Talapin, D. V. Many-Body Effects in Nanocrystal Superlattices: Departure from Sphere Packing Explains Stability of Binary Phases. *Journal of the American Chemical Society* **137**, 4494-4502, doi:10.1021/jacs.5b00839 (2015).
83 Steinhardt, P. J., Nelson, D. R. & Ronchetti, M. Bond-orientational order in liquids and glasses. *Physical Review B* **28**, 784-805, doi:10.1103/PhysRevB.28.784 (1983).
84 Romano, F., Sanz, E. & Sciortino, F. Crystallization of tetrahedral patchy particles in silico. *The Journal of Chemical Physics* **134**, 174502, doi:10.1063/1.3578182 (2011).
85 Weeks, J. D., Chandler, D. & Andersen, H. C. Role of Repulsive Forces in Determining the Equilibrium Structure of Simple Liquids. *The Journal of Chemical Physics* **54**, 5237-5247, doi:10.1063/1.1674820 (1971).
86 Moroni, D., ten Wolde, P. R. & Bolhuis, P. G. Interplay between Structure and Size in a Critical Crystal Nucleus. *Physical Review Letters* **94**, 235703, doi:10.1103/PhysRevLett.94.235703 (2005).
87 Rein ten Wolde, P., Ruiz-Montero, M. J. & Frenkel, D. Numerical calculation of the rate of crystal nucleation in a Lennard-Jones system at moderate undercooling. *The Journal of Chemical Physics* **104**, 9932-9947, doi:10.1063/1.471721 (1996).
88 Zimmermann, N. E. R., Vorselaars, B., Quigley, D. & Peters, B. Nucleation of NaCl from Aqueous Solution: Critical Sizes, Ion-Attachment Kinetics, and Rates. *Journal of the American Chemical Society* **137**, 13352-13361, doi:10.1021/jacs.5b08098 (2015).
89 Gebauer, D., Völkel, A. & Cölfen, H. Stable Prenucleation Calcium Carbonate Clusters. *Science* **322**, 1819-1822, doi:10.1126/science.1164271 (2008).
90 Israelachvili, J. N. *Intermolecular and surface forces*. (Academic press, 2015).
91 Shevchenko, E. V., Talapin, D. V., O'Brien, S. & Murray, C. B. Polymorphism in AB13 Nanoparticle Superlattices: An Example of Semiconductor−Metal Metamaterials. *Journal of the American Chemical Society* **127**, 8741-8747, doi:10.1021/ja050510z (2005).
92 Ye, X., Chen, J. & Murray, C. B. Polymorphism in Self-Assembled AB6 Binary Nanocrystal Superlattices. *Journal of the American Chemical Society* **133**, 2613-2620, doi:10.1021/ja108708v (2011).
93 Chen, J., Ye, X. & Murray, C. B. Systematic Electron Crystallographic Studies of Self-Assembled Binary Nanocrystal Superlattices. *ACS Nano* **4**, 2374-2381, doi:10.1021/nn1003259 (2010).
94 Park, S. Y. *et al.* DNA-programmable nanoparticle crystallization. *Nature* **451**, 553-556, doi:10.1038/nature06508 (2008).
95 Nykypanchuk, D., Maye, M. M., van der Lelie, D. & Gang, O. DNA-guided crystallization of colloidal nanoparticles. *Nature* **451**, 549-552, doi:10.1038/nature06560 (2008).

96 Lu, F., Yager, K. G., Zhang, Y., Xin, H. & Gang, O. Superlattices assembled through shape-induced directional binding. *Nature Communications* **6**, 6912, doi:10.1038/ncomms7912 (2015).
97 Marino, E., Bharti, H., Xu, J., Kagan, C. R. & Murray, C. B. Nanocrystal Superparticles with Whispering-Gallery Modes Tunable through Chemical and Optical Triggers. *Nano Letters*, doi:10.1021/acs.nanolett.2c01011 (2022).
98 Kumar, P. *et al.* Photonically active bowtie nanoassemblies with chirality continuum. *Nature* **615**, 418-424, doi:10.1038/s41586-023-05733-1 (2023).
99 Neuhaus, S. J., Marino, E., Murray, C. B. & Kagan, C. R. Frequency Stabilization and Optically Tunable Lasing in Colloidal Quantum Dot Superparticles. *Nano Letters* **23**, 645-651, doi:10.1021/acs.nanolett.2c04498 (2023).
100 Vanmaekelbergh, D. *et al.* Shape-Dependent Multiexciton Emission and Whispering Gallery Modes in Supraparticles of CdSe/Multishell Quantum Dots. *ACS Nano* **9**, 3942-3950, doi:10.1021/nn507310f (2015).
101 Poyser, C. L. *et al.* Coherent Acoustic Phonons in Colloidal Semiconductor Nanocrystal Superlattices. *ACS Nano* **10**, 1163-1169, doi:10.1021/acsnano.5b06465 (2016).
102 Bozyigit, D. *et al.* Soft surfaces of nanomaterials enable strong phonon interactions. *Nature* **531**, 618-622, doi:10.1038/nature16977 (2016).
103 Voznyy, O. *et al.* Machine Learning Accelerates Discovery of Optimal Colloidal Quantum Dot Synthesis. *ACS Nano* **13**, 11122-11128, doi:10.1021/acsnano.9b03864 (2019).
104 Guntern, Y. T. *et al.* Synthetic Tunability of Colloidal Covalent Organic Framework/Nanocrystal Hybrids. *Chemistry of Materials* **33**, 2646-2654, doi:10.1021/acs.chemmater.1c00501 (2021).
105 Park, J. *et al.* Ultra-large-scale syntheses of monodisperse nanocrystals. *Nature Materials* **3**, 891-895, doi:10.1038/nmat1251 (2004).
106 Ye, X., Fei, J., Diroll, B. T., Paik, T. & Murray, C. B. Expanding the Spectral Tunability of Plasmonic Resonances in Doped Metal-Oxide Nanocrystals through Cooperative Cation–Anion Codoping. *Journal of the American Chemical Society* **136**, 11680-11686, doi:10.1021/ja5039903 (2014).
107 Moreels, I. *et al.* Size-Dependent Optical Properties of Colloidal PbS Quantum Dots. *ACS Nano* **3**, 3023-3030, doi:10.1021/nn900863a (2009).
108 Bressler, I., Kohlbrecher, J. & Thunemann, A. F. SASfit: a tool for small-angle scattering data analysis using a library of analytical expressions. *Journal of Applied Crystallography* **48**, 1587-1598, doi:doi:10.1107/S1600576715016544 (2015).
109 Langford, J. I. & Wilson, A. J. C. Scherrer after sixty years: A survey and some new results in the determination of crystallite size. *Journal of Applied Crystallography* **11**, 102-113, doi:doi:10.1107/S0021889878012844 (1978).
110 Anderson, J. A., Glaser, J. & Glotzer, S. C. HOOMD-blue: A Python package for high-performance molecular dynamics and hard particle Monte Carlo simulations. *Computational Materials Science* **173**, 109363, doi:https://doi.org/10.1016/j.commatsci.2019.109363 (2020).
111 Noya, E. G., Conde, M. M. & Vega, C. Computing the free energy of molecular solids by the Einstein molecule approach: Ices XIII and XIV, hard-dumbbells and a patchy model of proteins. *The Journal of Chemical Physics* **129**, 104704, doi:10.1063/1.2971188 (2008).

112 Frenkel, D. & Ladd, A. J. C. New Monte Carlo method to compute the free energy of arbitrary solids. Application to the fcc and hcp phases of hard spheres. *The Journal of Chemical Physics* **81**, 3188-3193, doi:10.1063/1.448024 (1984).
113 Martyna, G. J., Tobias, D. J. & Klein, M. L. Constant pressure molecular dynamics algorithms. *The Journal of Chemical Physics* **101**, 4177-4189, doi:10.1063/1.467468 (1994).
114 Phillips, C. L., Anderson, J. A. & Glotzer, S. C. Pseudo-random number generation for Brownian Dynamics and Dissipative Particle Dynamics simulations on GPU devices. *Journal of Computational Physics* **230**, 7191-7201, doi:https://doi.org/10.1016/j.jcp.2011.05.021 (2011).
115 Barker, J. A. & Henderson, D. What is "liquid"? Understanding the states of matter. *Reviews of Modern Physics* **48**, 587-671, doi:10.1103/RevModPhys.48.587 (1976).
116 Ramasubramani, V. *et al.* freud: A software suite for high throughput analysis of particle simulation data. *Computer Physics Communications* **254**, 107275, doi:https://doi.org/10.1016/j.cpc.2020.107275 (2020).
117 Stukowski, A. Visualization and analysis of atomistic simulation data with OVITO–the Open Visualization Tool. *Modelling and Simulation in Materials Science and Engineering* **18**, 015012, doi:10.1088/0965-0393/18/1/015012 (2009).
118 Adorf, C. S., Dodd, P. M., Ramasubramani, V. & Glotzer, S. C. Simple data and workflow management with the signac framework. *Computational Materials Science* **146**, 220-229, doi:https://doi.org/10.1016/j.commatsci.2018.01.035 (2018).
119 Ramasubramani, V., Adorf, C., Dodd, P., Dice, B. & Glotzer, S. in *Proceedings of the Python in Science Conference.*
120 Towns, J. *et al.* XSEDE: Accelerating Scientific Discovery. *Computing in Science & Engineering* **16**, 62-74, doi:10.1109/MCSE.2014.80 (2014).

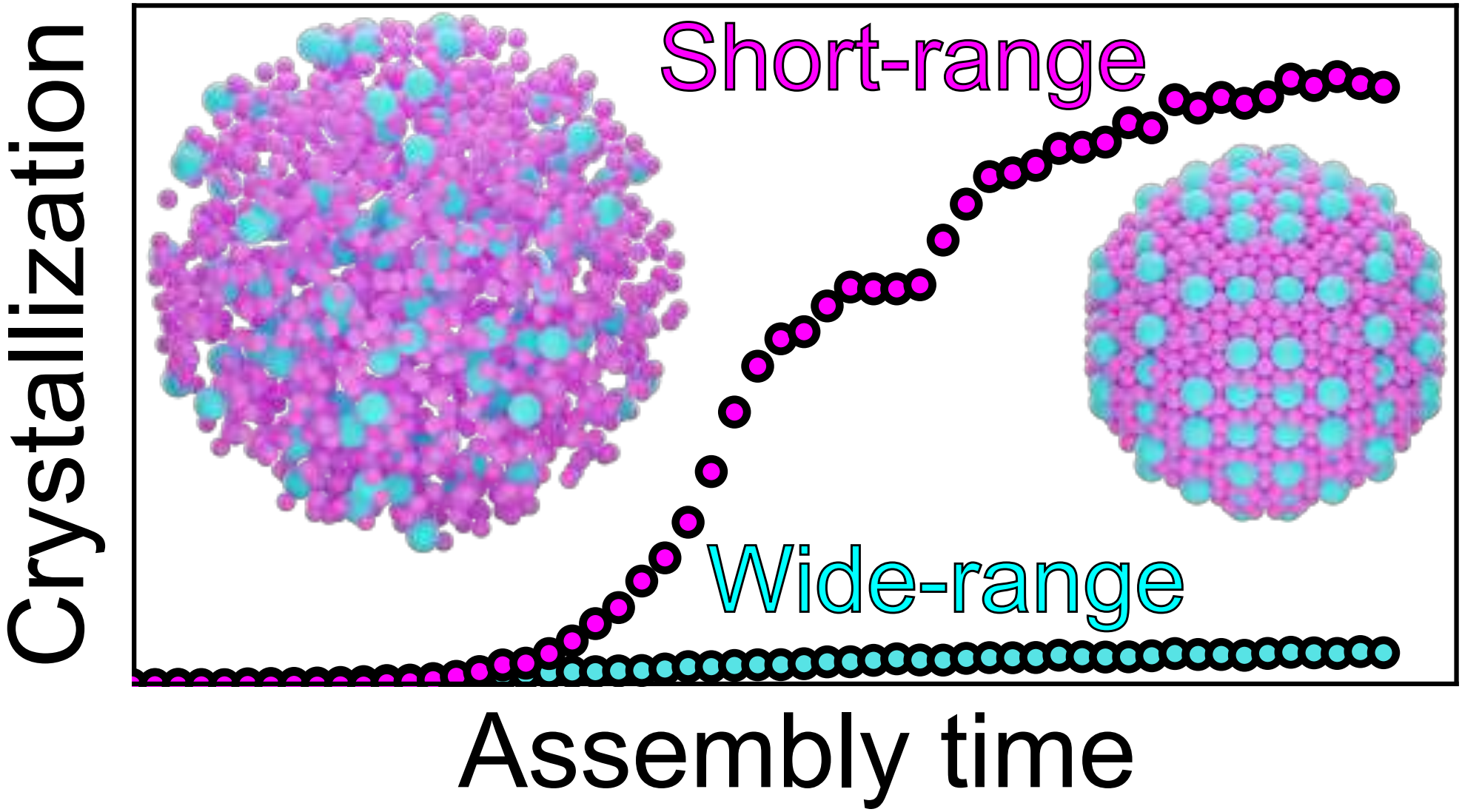
Crystallization
Short-range
Wide-range
Assembly time

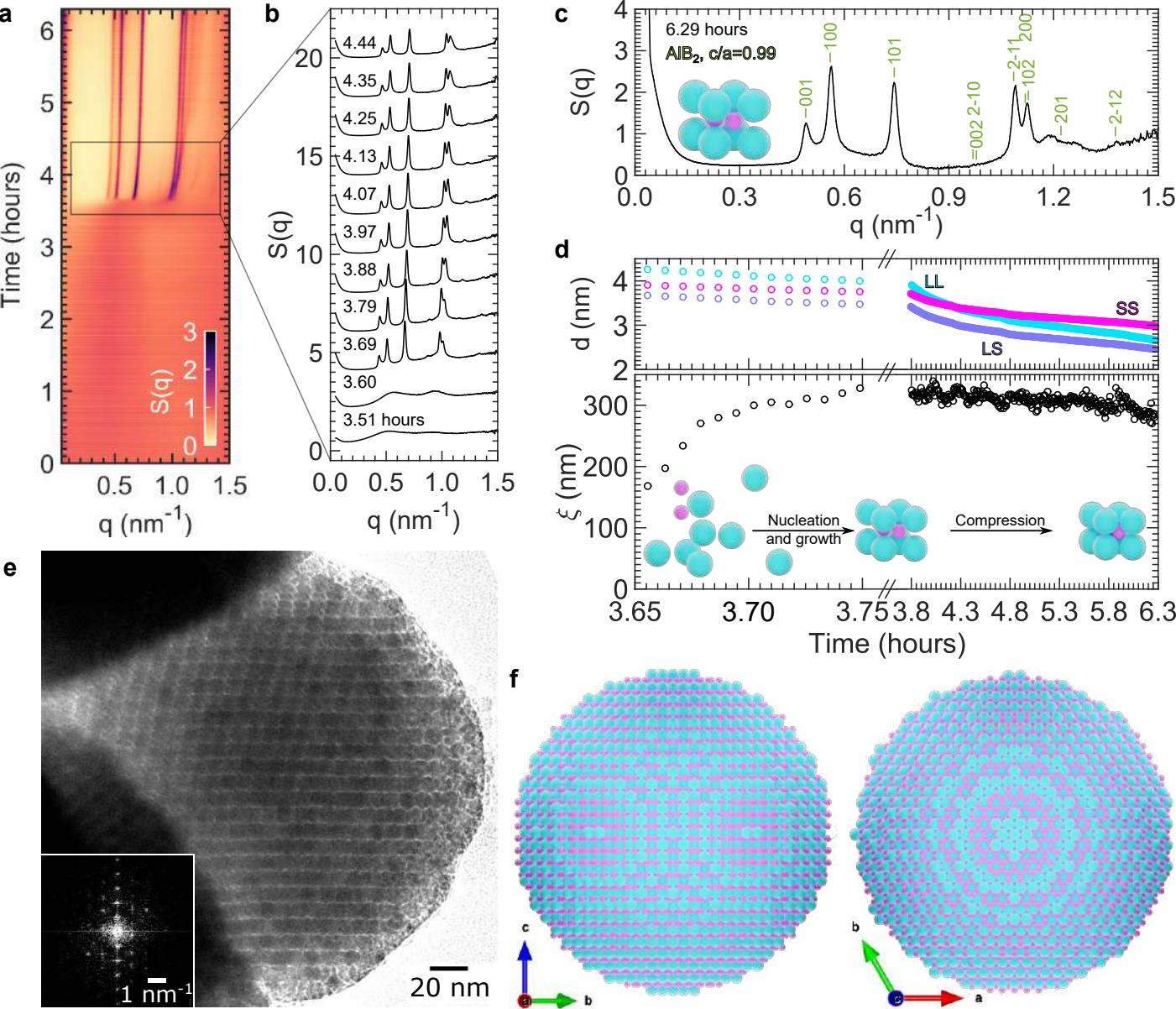
a
Time (hours)
q (nm^{-1})
S(q)
b
S(q)
4.44
4.35
4.25
4.13
4.07
3.97
3.88
3.79
3.69
3.60
3.51 hours
q (nm^{-1})
c
6.29 hours
AlB$_2$, c/a=0.99
S(q)
001
100
101
002 2-10
2-11
200
102
201
2-12
q (nm^{-1})
d
d (nm)
LL
SS
LS
ξ (nm)
Nucleation and growth
Compression
Time (hours)
e
1 nm^{-1}
20 nm
f
c
a
b
b
a

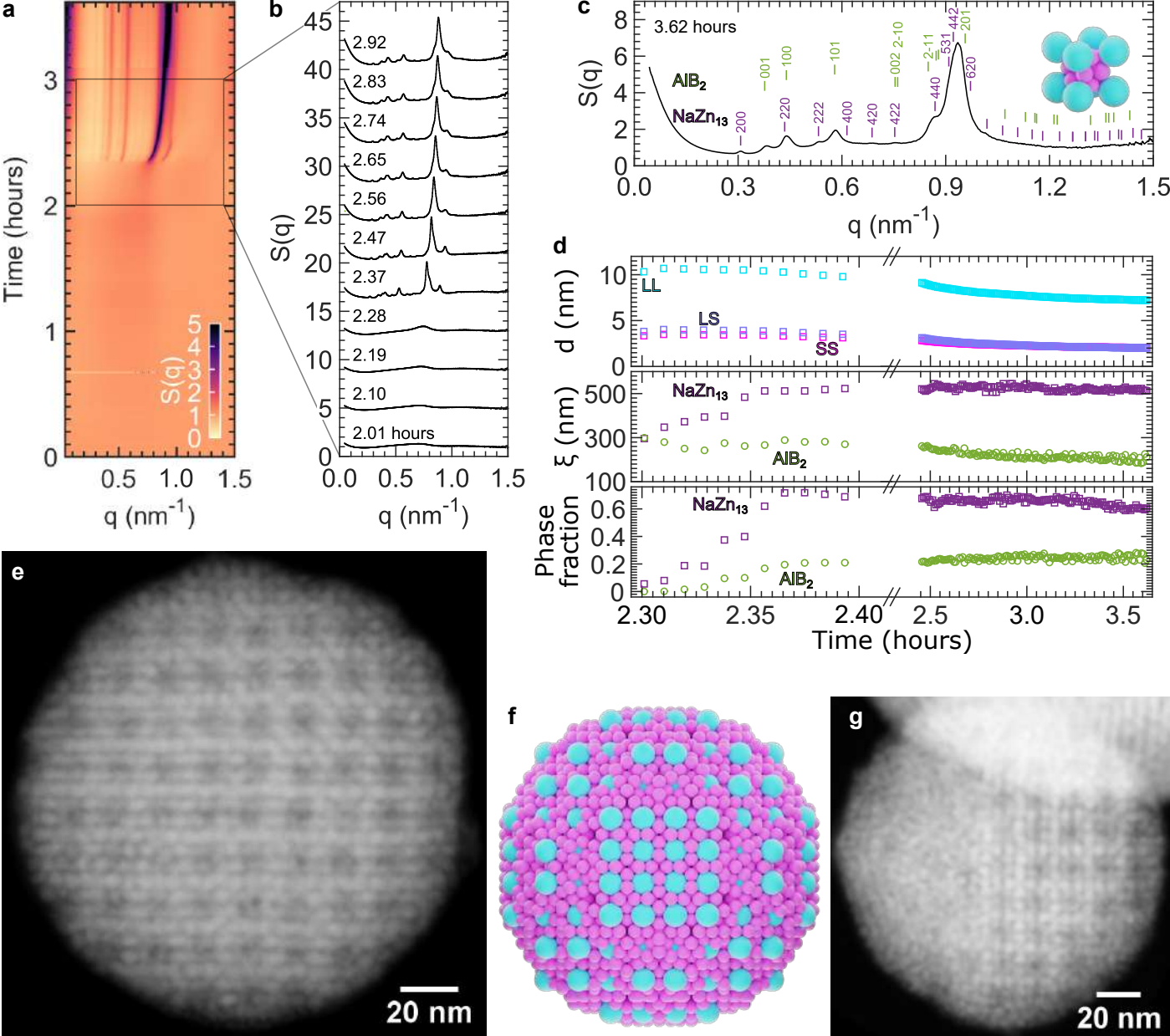
a
Time (hours)
q (nm^{-1})
S(q)
b
S(q)
2.92
2.83
2.74
2.65
2.56
2.47
2.37
2.28
2.19
2.10
2.01 hours
q (nm^{-1})
c
3.62 hours
AlB$_2$
NaZn$_{13}$
001
100
200
220
101
222
400
420
002 2-10
422
2-11
531
440
442
201
620
S(q)
q (nm^{-1})
d
LL
LS
SS
d (nm)
NaZn$_{13}$
AlB$_2$
ξ (nm)
NaZn$_{13}$
AlB$_2$
Phase fraction
Time (hours)
e
20 nm
f
g
20 nm

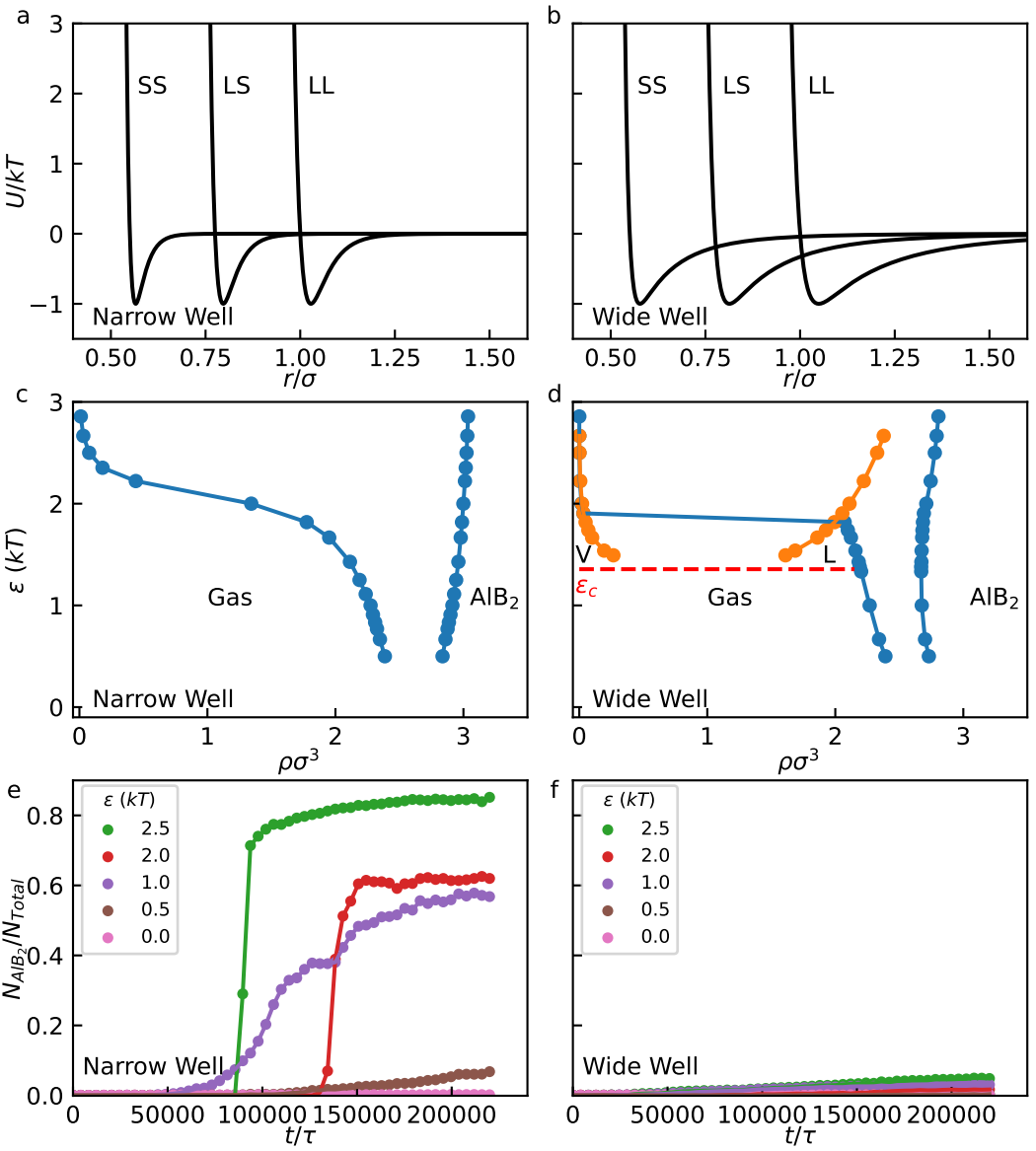
a
b
SS
LS
LL
U/kT
Narrow Well
Wide Well
r/σ
c
d
ε (kT)
Gas
AlB2
V
L
εc
ρσ3
e
f
ε (kT)
2.5
2.0
1.0
0.5
0.0
NAlB2/NTotal
t/τ

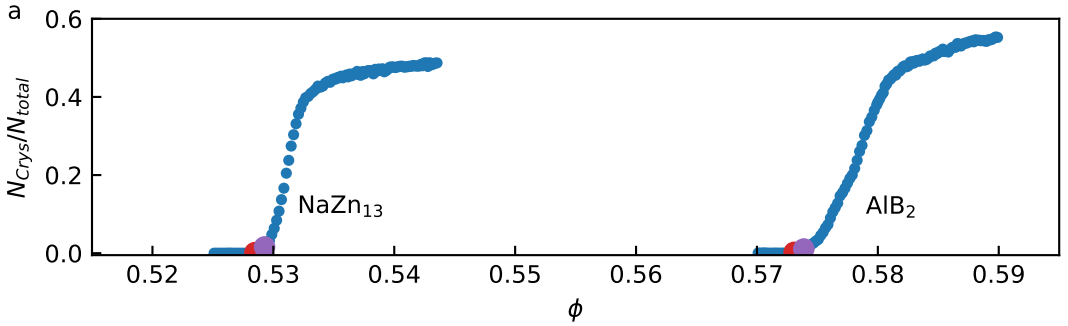
a
0.6
0.4
0.2
0.0
N_{Crys}/N_{total}
NaZn$_{13}$
AlB$_2$
0.52
0.53
0.54
0.55
0.56
0.57
0.58
0.59
ϕ

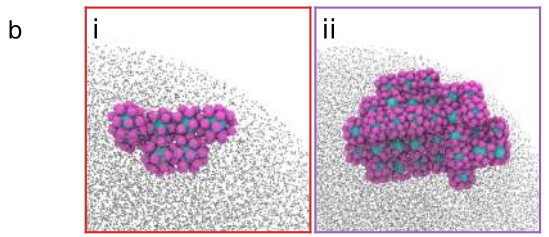
b
i
ii

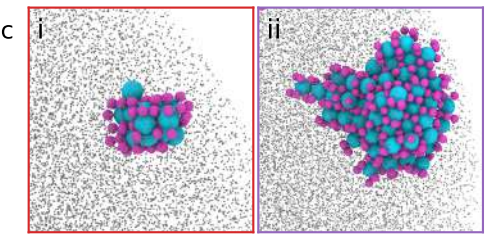
c
i
ii

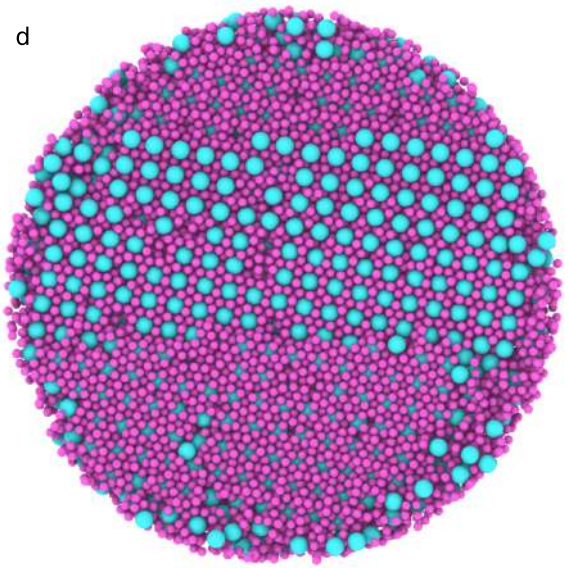
d

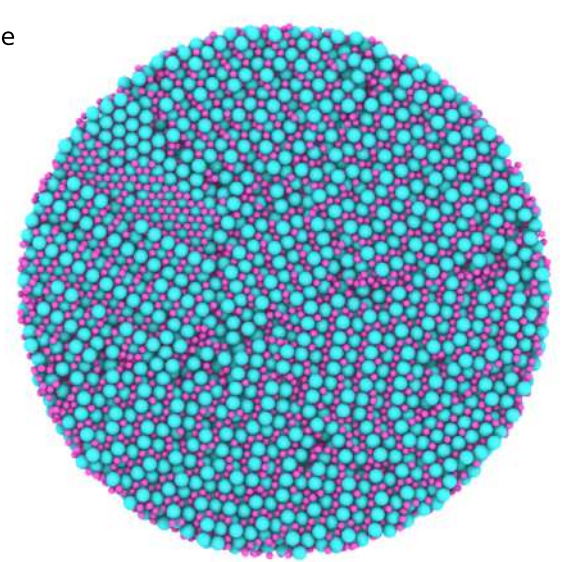
e